

Chemical abundances of Seyfert 2 AGNs – IV. Composite models calculated by photoionization + shocks

O. L. Dors¹,¹★ M. Contini,²★ R. A. Riffel³,³ E. Pérez-Montero,⁴ A. C. Krabbe,¹ M. V. Cardaci^{5,6} and G. F. Hägele^{5,6}

¹Universidade do Vale do Paraíba, Av. Shishima Hifumi, 2911, Cep 12244-000 São José dos Campos, SP, Brazil

²School of Physics and Astronomy, Tel Aviv University, Tel Aviv 69978, Israel

³Universidade Federal de Santa Maria, Av. Roraima 1000, Cep 97105-900 Santa Maria, Brazil

⁴Instituto de Astrofísica de Andalucía, Camino Bajo de Huétor s/n, Aptdo. 3004, E-18080 Granada, Spain

⁵Instituto de Astrofísica de La Plata (CONICET-UNLP), La Plata, Avenida Centenario (Paseo del Bosque) S/N, B1900FWA, Argentina

⁶Facultad de Ciencias Astronómicas y Geofísicas, Universidad Nacional de La Plata, Paseo del Bosque s/n, 1900 La Plata, Argentina

Accepted 2020 November 24. Received 2020 November 23; in original form 2020 August 26

ABSTRACT

We build detailed composite models of photoionization and shock ionization based on the SUMA code to reproduce emission lines emitted from the Narrow Line Regions (NLR) of Seyfert 2 nuclei. The aim of this work is to investigate diagram active galactic nucleus (AGN) positions according to shock parameters, shock effects on the gas temperature and ionization structures and derive a semi-empirical abundance calibration based on emission-line ratios little sensitive to the shock presence. The models were used to reproduce optical ($3000 < \lambda(\text{\AA}) < 7000$) emission line intensities of 244 local ($z \lesssim 0.4$) Seyfert 2s, whose observational data were selected from Sloan Digital Sky Survey DR7. Our models suggest that shocks in Seyfert 2 nuclei have velocities in the range of $50\text{--}300 \text{ km s}^{-1}$ and imply a narrower metallicity range ($0.6 \lesssim (Z/Z_{\odot}) \lesssim 1.6$) than those derived using pure photoionization models. Our results indicate that shock velocity in AGNs cannot be estimated using standard optical line ratio diagrams, based on integrated spectra. Our models predict a different temperature structure and O^+/O and O^{2+}/O fractional abundances throughout the NLR clouds than those derived from pure photoionization models, mainly in shock-dominated objects. This suggests that, in order to minimize the shock effects, the combination of emission-lines emitted by ions with similar intermediate ionization potential could be good metallicity indicators. Finally, we derive two calibrations between the N/O abundance ratio and the $\text{N}_2\text{O}_2 = \log([\text{N II}]\lambda 6584/[\text{O II}]\lambda 3727)$ and $\text{N}_2 = \log([\text{N II}]\lambda 6584/\text{H}\alpha)$ indexes which agree with that derived from pure photoionization models.

Key words: galaxies: abundances – galaxies: active – galaxies: evolution – galaxies: formation – galaxies: ISM – galaxies: nuclei – galaxies: Seyfert.

1 INTRODUCTION

Active galactic nuclei (AGNs) and star-forming regions (SFs) present in their spectra prominent emission lines observed from X-ray to radio wavelengths. The relative intensities and the profiles of these lines reveal the properties of the gas phase, such as chemical abundances, ionization degree, kinematics, etc. Since AGNs and SFs are thought to be ubiquitous in the Universe from their very first stages, investigating the physics underlying these objects is crucial to understand their role in the cosmic evolution of galaxies.

The seminal paper by Baldwin, Phillips & Terlevich (1981) allowed the first taxonomy of emitter objects through diagnostic diagrams (hereafter BPT diagrams) containing optical emission-line ratios (see also Veilleux & Osterbrock 1987; Kewley et al. 2001; Kauffmann et al. 2003; Pérez-Montero et al. 2013). BPT diagrams show that AGNs (and most planetary nebulae, see Frew & Parker 2010) exhibit higher line ratios (e.g. $[\text{O III}]\lambda 5007/\text{H}\beta$

and $[\text{N II}]\lambda 6584/\text{H}\alpha$) than those of SFs. The difference between line intensity ratios of AGNs, on the scenario of photoionization due to radiation emitted by gas accretion into a supermassive black hole (SMBH), is mainly due to a much harder ionizing spectral energy distribution (SED) in combination with a higher ionization degree (e.g. Pérez-Montero et al. 2019) and to a larger metallicity in AGN hosts (e.g. Stasińska 1984; Storch-Bergmann & Pastoriza 1990; Storch-Bergmann et al. 1998; Groves, Heckman & Kauffmann 2006; Feltre, Charlot & Gutkin 2016). However, high values of line intensity ratios are also obtained adopting shock dominated models with relatively high shock velocities (V_s), because the higher V_s the higher $[\text{O III}]\lambda 5007/\text{H}\beta$ ratio (e.g. Spence et al. 2016). Therefore, in a more realistic physical frame, models built to reproduce observational line intensity ratios should account for a composite ionization source (AGN+shock), which lead to more reliable results than those obtained by pure photoionization or pure shock models.

Collisional ionization and heating of the gas by the shocks contribute to the line intensities measured in the spectra of both AGN hosts and SF galaxies (Aldrovandi & Contini 1984; Dopita

* E-mail: olidors@univap.br (OLD); marcel@wise.tau.ac.il (MC)

& Sutherland 1995, 1996). Shocks have a strong influence on the gas properties (e.g. Viegas-Aldrovandi & Contini 1989; Dopita & Sutherland 1996; Allen et al. 2008), in particular, on the gas density, temperature downstream, cooling rates throughout the clouds, etc. Consequently, they affect the emission lines. The element abundances, the flux from the active centre (AC), the dust-to-gas ratios, etc., characterize the gas in pre-shock regions. Shock velocities (or a more turbulent gas) generated by outflows in AGNs (e.g. Rosario et al. 2010; Riffel, Storchi-Bergmann & Riffel 2014; Wylezalek et al. 2020) are higher than those in SF galaxies which originate mainly from stellar winds of young massive stars (e.g. Dyson 1979; Rozas et al. 2007; Westmoquette et al. 2007; Amorín et al. 2012; Bosch et al. 2019). Therefore, the optical line profiles observed, for instance, in narrow line regions (NLRs) of Seyfert 2 AGNs show full-width at half-maximum (FWHM) ranging from 200 to 1000 km s⁻¹ (e.g. Koski 1978; Vaona et al. 2012; Zhang, Liang & Hammer 2013) while those measured in SFs regions are $\lesssim 200$ km s⁻¹ (e.g. Melnick et al. 1977; Skillman, Balick & ApJ 1984; Relaño et al. 2005; Hägele et al. 2013; Bresolin et al. 2020). The FWHM of optical emission lines is a good tracer of the shock velocities (e.g. Contini 2012).

Regarding the metallicity, shocks in NLRs can be one of the causes behind the T_e -problem in Seyfert 2 nuclei. In fact, Dors et al. (2015) showed that the determination of the metallicity Z (in terms of the O/H abundance) from the direct measurement of the electron temperature¹ (T_e), provides a reliable – even if approximated – method for SFs (see e.g. Pilyugin 2003; Hägele, Pérez-Montero & Díaz A. I. et al. 2006; Hägele et al. 2008; Contini 2014) but produces unrealistic low Z (see also Dors, Freitas-Lemes & Amôres E. B. et al. 2020a) in the NLRs of Seyfert 2 galaxies. Sub-solar metallicities are obtained as a consequence of the high values of the electron temperature ($T_e > 20\,000$ K) in the NLRs which translates into low Z . Heckman & Balick (1979) pointed out that such high temperatures require another source of energy in addition to photoionization, e.g. the presence of shocks (see also Zhang et al. 2013; Contini 2017). Dors et al. (2020b) presented a new formalism of the T_e -method for Seyfert 2, i.e. a new relation between the temperature of the low (t_2) and high (t_3) ionization gas zones, which is different from those commonly used for chemical abundance studies in the H II regions (e.g. Garnett 1992; Hägele et al. 2008; Pérez-Montero 2014). Despite the use of this new methodology produces a cut down of the difference between the O/H abundances estimated through the T_e -method and those obtained by pure photoionization models to ~ 0.2 dex, some caveats still prevent the use of the T_e -method for AGNs. For instance, T_e can be calculated from $R_{O3} = ([O\ III](\lambda 4959 + \lambda 5007)/\lambda 4363)$ line ratio in the range of $700 \gtrsim R_{O3} \gtrsim 30$ which corresponds to $7000 \lesssim T_e(K) \lesssim 23\,000$ (Hägele et al. 2008). However, R_{O3} lower than 30 is derived in some Seyfert 2 (e.g. Komossa & Schulz 1997; Nagao, Murayama & Taniguchi 2001; Vaona et al. 2012), indicating $T_e > 23\,000$ K and a limited use of the T_e -method for this class of objects. Moreover, the discrepancy between T_e calculated from measurements of R_{O3} and those predicted by pure photoionization models is systematic, meaning that it increases (from ~ 0 to $\sim 11\,000$ K) when the values derived by the T_e -method increase (varying in the 11 000–20 000 range; Dors et al. 2020b). This indicates that another mechanism is acting in NLRs.

Shocks with velocities $V_s \lesssim 400$ km s⁻¹ have been proposed to be at work in the NLR of Seyfert 2s galaxies (e.g. Contini 2017). High T_e throughout the emitting clouds are mainly due, as previously

reported, to the presence of shocks (e.g. Dors et al. 2015; Contini 2017). They can produce some uncertainties in the use of the T_e method. A basic difference between radiation-dominated and shock-dominated models consists in the profile of T_e in the recombination region of the gas within the emitting nebula because the cooling rate downstream of the shock front is strengthened by compression (Contini 2017).

The main goal of this paper is to investigate shock effects on the NLR gas of Seyfert 2 galaxies, analysing the loci of the corresponding line ratios in BPT diagrams according to shock parameters and abundances, investigating the influence of shocks on temperature and ionization structure and deriving an abundance calibration based on emission-line ratios less sensitive to shock. Therefore, we adopt composite models (photoionization + shock) using the SUMA code (Viegas-Aldrovandi & Contini 1989) in order to reproduce the optical narrow emission lines of 244 Seyfert 2 nuclei whose data were taken from the Sloan Digital Sky Survey (SDSS; York et al. 2000) by Dors et al. (2020a). This paper is organized as follows: in Section 2 the methodology (observational data and models) is presented; in Section 3 the results of detailed modelling of the spectra are presented, while the discussion and conclusion remarks are given in Sections 4 and 5, respectively.

2 METHODOLOGY

2.1 Observational data

We consider optical narrow emission line intensities ($3600 < \lambda(\text{\AA}) < 7200$) of a sample of Seyfert 2 galaxies compiled by Dors et al. (2020a). These data were taken from SDSS-DR7 (York et al. 2000; Abazajian, Adelman-McCarthy & Agüeros M. A. et al. 2009) and the emission line intensity measurements are made available by the MPA/JHU group.² To select the objects, Dors et al. (2020a) applied the criteria to separate AGN-like and SF-like objects proposed by Kewley et al. (2001, 2006) and Pérez-Montero et al. (2013) and based on BPT diagrams. After selecting a sample of AGNs, Dors et al. (2020a) carried out a cross-correlation between basic information from the SDSS-DR7 and in NED/IPAC³ (NASA/IPAC Extragalactic Data base) catalogues in order to obtain only Seyfert 2 AGNs. This procedure eliminates from the sample SFs, star-forming galaxies, Seyfert 1 galaxies, quasars, and Planetary Nebulae.

The resulting sample consists of 463 Seyfert 2 AGNs with redshifts $z \lesssim 0.4$ and with stellar masses of the host galaxies (also taken from the MPA-JHU group) in the range of $9.4 \lesssim \log(M/M_\odot) \lesssim 11.6$. For our analysis, we considered several emission-line intensities measured by the MPA-JHU group, reddening corrected and expressed in relation to H β , including [O II] $\lambda 3726 + \lambda 3729$ (hereafter indicated as [O II] $\lambda 3727$), [Ne III] $\lambda 3869$, [O III] $\lambda 4363$, [O III] $\lambda 5007$, He I $\lambda 5876$, [O I] $\lambda 6300$, H α , [N II] $\lambda 6584$, [S II] $\lambda 6716$, [S II] $\lambda 6731$, and [Ar III] $\lambda 7135$ emission lines. The reader is referred to Dors et al. (2020a) for a complete description of this sample.

2.2 Composite models

We built models by using the SUMA code (Viegas-Aldrovandi & Contini 1989) in order to reproduce the observed spectra of each object of our sample. This code has the advantage of considering a combination of two ionization sources: the photoionization flux from

¹This method is referred as T_e -method or direct method.

²<https://wwwmpa.mpa-garching.mpg.de/SDSS/DR7/>

³ned.ipac.caltech.edu

the AC and collisional effects from the shock. A detailed description of the input parameters is given by Contini (2019) and a summary is presented in the following paragraphs.

(i) Ionization sources: The composite effect of photoionization from the AC and collisional ionization and heating from shocks are considered. The radiation emitted by the AC is represented by a power-law flux F in number of photons $\text{cm}^{-2} \text{s}^{-1} \text{eV}^{-1}$ at the Lyman limit, with spectral indices $\alpha_{\text{UV}} = -1.5$ and $\alpha_X = -0.7$. The flux F is measured at the innermost surface of the cloud, i.e. illuminated face of the cloud. The shock input parameters are: the shock velocity V_s , the atomic pre-shock density n_0 and the pre-shock magnetic field B_0 , which defines the hydrodynamical field. They are used in the solution of the Rankine–Hugoniot equations at the shock front and downstream. These equations are combined into the compression equation which leads to the calculations of the density profile downstream. We adopted for all the models $B_0 = 10^{-4} \text{G}$, which is suitable to the NLR of AGNs according to Beck (2012). It is worth mentioning that the magnetic field B_0 has an important role in models accounting for the shock. The stronger B_0 , the lower the compression downstream. Therefore, lower densities are compensated by a lower B_0 . The gas reaches a maximum temperature in the immediate post-shock region $T_e \sim 1.5 \times 10^5 (V_s/100 \text{ km s}^{-1})^2$. T_e decreases downstream following the cooling rate of the gas.

(ii) Geometry: The models adopt gaseous clouds in a plane-parallel geometry. The geometrical thickness D of the clouds determines whether each model is radiation-bounded or matter-bounded. D is calculated consistently with the physical conditions and element abundances of the emitting gas.

(iii) Elemental abundances: The code considers, initially, solar abundances (Grevesse & Sauval 1988) for all the elements (H, He, C, N, O, Ne, Mg, Si, S, Cl, Ar, and Fe), which are varied in the models in order to reproduce the observed line ratios. We adopted the solar He/H relative abundance (in number of atoms, Ferland et al. 2017) of 0.1 for all the models.

(iv) Dust: Dust is present in the emitting clouds. It is characterized by the dust-to-gas ratio d/g and by the initial grain radius a_{gr} , which are constrained by fitting the continuum spectral energy distribution (SED). We adopt in the modelling of the present AGN survey $d/g = 10^{-14}$ by number and $a_{\text{gr}} = 1 \mu\text{m}$ because values in these ranges lead to the best fit of the AGN SED observed through a wide range of wavelengths (see e.g. Contini 2018).

We calculate for each object of our sample a large grid of models, varying the input parameters V_s , n_0 , D , F , N/H, O/H, and S/H, in a consistent way (i.e. by considering the effect of each of them on the different line ratios), until a fine tune of all the line ratios to the data has been obtained. The best-fitting models were finally selected by comparing the calculated to the observed line ratios and by constraining the precision of the fit by discrepancies that are set at 20 per cent for the strongest lines (e.g. [O II] $\lambda 3727$, [O III] $\lambda 5007$) and 50 per cent for the weakest lines (e.g. [O III] $\lambda 4363$). We verify that the range of parameters of the best-fitting models do not differ more than 10 percent. Thus, this value is adopted as uncertainty in the derived parameters from the composite models. In order to show the fit procedure, in Fig. 1, two BPT diagnostic diagrams, we show a selected portion of the grids which were used to reproduce the spectra, for sample, of the objects number 31 ($V_s \sim 200 \text{ km s}^{-1}$) and 359 ($V_s \sim 80 \text{ km s}^{-1}$). The best-fitting model represented by the large open circle is slightly displaced from the observed point (represented by a cross) in order to reproduce as much as possible all the line ratios (see Table 1). Not always the results follow smoothly and monotonically the input parameters, in particular the element

abundances. This is due to the fact that all of them participate differently to the cooling rate throughout the cloud. Particularly, oxygen is a strong coolant.

In this work, the O/H, N/H, and S/H relative abundances were varied in the models in order to reproduce the correspondent observed lines. On the contrary, Ne/H and Ar/H were kept constant in the models, i.e. the solar values were adopted for these elements. This has a small effect on the fitting models as they do not dominate the cooling rate downstream as much as N, O, and S.

Contini & Viegas (2001) presented a grid of composite models for narrow-line regions of active galaxies calculated with the SUMA code, taking into account different values of shock velocities, pre-shock densities, geometrical thickness of the clouds and ionizing radiation intensities in a large range. Based on this large grid, they found that if the flux from the AC is low ($F \leq 10^9 \text{ ph cm}^{-2} \text{s}^{-1} \text{eV}^{-1}$), a shock-dominated regime is found. Contini & Viegas (2001) also showed that the [O III]/[O II] line ratio is much more sensitive to the intensity of the flux radiation from the AC than to the shock velocities, being shock-dominated models characterized by relatively high $[(\text{[O II]}\lambda 3727)/(\text{[O III]}\lambda 5007) \gtrsim 1]$ line ratios. The ionization parameter U can be obtained from the parameter F by $U = [F/(n c (\alpha - 1))] \times [(E_H)^{-\alpha+1} - (E_C)^{-\alpha+1}]$ (see Contini & Aldrovandi 1983), where E_H is hydrogen ionization potential and E_C is the high energy cutoff, n the density, α the spectral index, and c the speed of light.

In Fig. 2, we present three BPT diagrams containing the emission-line ratio intensities of the observational sample and those predicted by the grid of composite models built by Contini & Viegas (2001). The model predictions are discriminated in terms of the shock velocity (V_s , in km s^{-1}) as indicated in the diagrams. Since the models of this grid consider only solar metallicity, we have added the results calculated for the grids adopted for m31 and m359 which include different values for N/H, O/H, and S/H, i.e. composite model results with a range of metallicity ($0.4 \lesssim (Z/Z_\odot) \lesssim 1.6$). Fig. 2 shows that the models cover very well the region occupied by the observations.

2.3 Detailed model approach

Most of the studies carried out to derive metallicity or abundances in AGNs are either based on theoretical calibrations from photoionization model sequences (e.g. Storchi-Bergmann et al. 1998; Dors et al. 2014) or on comparisons between model predicted and observational line-intensity ratios in diagnostic diagrams (e.g. Nagao, Maiolino & Marconi 2006; Feltre et al. 2016; Castro et al. 2017; Dors et al. 2019; Carvalho et al. 2020). The main problem in using photoionization model sequences is that, in most cases, it is assumed fixed relations for the N–O and S–O abundances, which can produce very uncertain abundance results (Pérez-Montero & Contini 2009), mainly because after the oxygen, the nitrogen and the sulphur are the main coolant elements in the nebular gas. Moreover, the above abundance relations are poorly known in AGNs (see Dors et al. 2017, 2019).

In this sense, the use of detailed modelling (e.g. Contini 2017; Dors et al. 2017) or Bayesian-like comparisons (e.g. Pérez-Montero et al. 2019) circumvent this problem because not fixed relations between the N, S, and O abundances are assumed, producing a more accurate solution for the nebular thermal equilibrium and, consequently, more reliable abundances. Although in the detailed models used in this work a fixed slope for the power law representing the SED and a fixed dust-to-gas ratio were assumed, Feltre et al. (2016) showed that these parameters have a secondary influence on the model predicted emission lines.

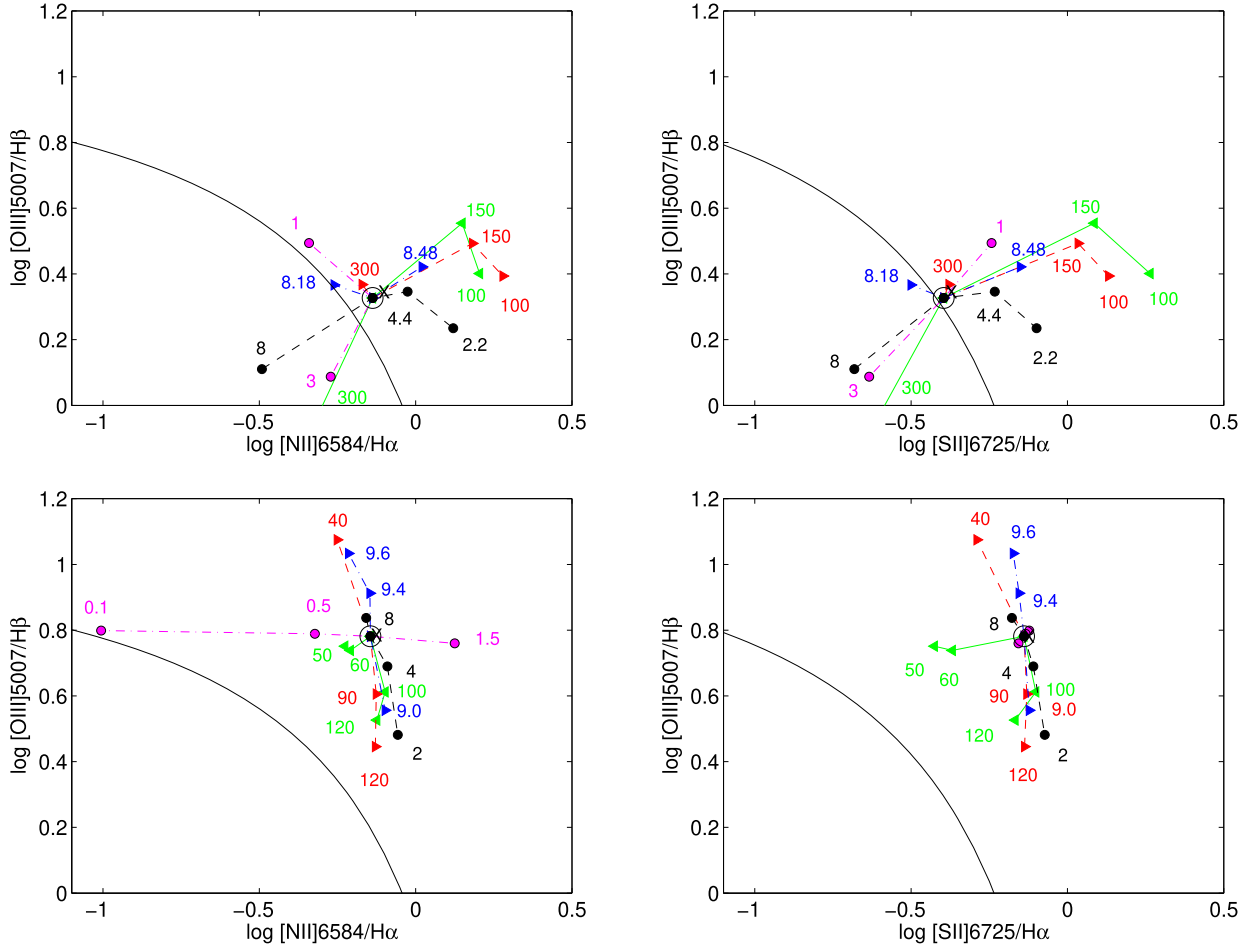


Figure 1. Diagnostic diagrams showing the fit procedure for two objects m31 (top panels) and m359 (bottom panels) of our sample (see Section 2.1). Curves represent the criteria proposed by Kewley et al. (2001) and Pérez-Montero et al. (2013) to separate AGN-like from H II-like objects. The emission line [S II] λ 6725 represents the sum of the intensities of λ 6716 and λ 6731. The lines show composite model predictions considering different input parameters of the grid, i.e. for V_s (green solid line), n_0 (red dashed line), $\log(F)$ (dot-dashed blue line), N/H (magenta solid line), and O/H (black dashed line). The numbers near green triangles give the V_s values in km s^{-1} , near red triangles the n_0 values in cm^{-3} , near blue triangles the $\log(F)$ values. The black filled circles connected by a solid line show the abundance ratios N/H (in 10^{-4} units), those connected by dashed lines show the O/H abundance ratios (in 10^{-4} units). The open black circle represents the model selected which best reproduces the data.

Table 1. De-reddened observed (Obs.) and predicted (Mod.) fluxes (relative to $H\beta = 1.00$) for two of the objects in our sample of Seyfert 2 nuclei. The observed values are listed in the lines with the identification of each object. The predicted values are listed in the lines starting with the label m . The stellar mass and redshift of each object are listed in the full table, available as supplementary material. In cases which a line was not measured its value is referred to 0.00.

Object		[O II] λ3727	[Ne III] λ3869	[O III] λ4363	[O III] λ4959+λ5007	He I λ5876	[O I] λ6300	H α λ6563	[N II] λ6584	[S II] λ6716	[S II] λ6731	[Ar III] λ7135
3	J000819.72–000002.7	2.58	0.00	0.00	2.77	0.00	0.27	2.86	2.37	0.84	0.35	0.14
m3	–	2.90	0.75	0.45	2.76	0.10	0.30	3.07	2.20	0.43	0.75	0.10
4	J000908.27–011013.8	1.64	0.73	0.00	2.13	0.01	0.31	2.86	2.37	0.78	0.27	0.00
m4	–	1.52	0.51	0.45	2.00	0.13	0.67	3.05	2.50	0.50	0.80	0.83

3 RESULTS

In Fig. 3, the observed emission-line ratios are compared with those predicted by detailed modelling with SUMA for the 463 objects. The [O III] λ 4363 line was measured only in 280/463 objects. In this figure we also show as dashed lines a typical observational uncertainty of 20 and 50 per cent for strong and weak emission-line ratios, respectively (e.g. Kraemer et al. 1994). A good agreement between the strong [O II] λ 3727, [O III] λ 5007, and [N II] λ 6584 emission lines

can be seen. The sum of the [S II] λ 6716 and λ 6731 lines is well reproduced by the models.

From the 463 objects of our sample, we obtain reliable model solutions for all the strong emission lines [O II] λ 3727, [O III] λ 5007, [N II] λ 6584, and [S II] λ 6716+ λ 6725 in 244 galaxies. In Table 1 the observed intensity ratios are compared with the calculated ones (relative to $H\beta = 1$), while the model parameters selected from the best fit to the observed data are listed in Table 2. The

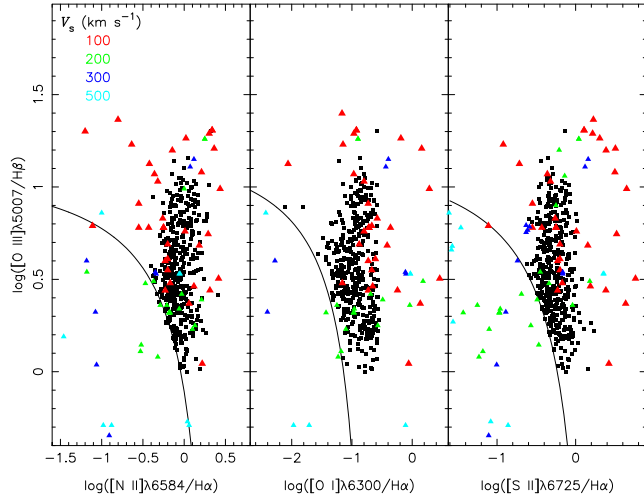


Figure 2. Diagnostic diagrams $[\text{O III}]\lambda 5007/\text{H}\beta$ versus $[\text{N II}]\lambda 6584/\text{H}\alpha$, versus $[\text{O I}]\lambda 6300/\text{H}\alpha$ and versus $[\text{S II}]\lambda 6725/\text{H}\alpha$. The black points represent the 463 objects of our sample. The coloured points represent results of the composite model grid built by Contini & Viegas (2001) and results calculated for the objects of our sample m31 and m359, which include different values for N/H, O/H, and S/H, i.e. composite model results with a given range of metallicity ($0.4 \lesssim (Z/Z_\odot) \lesssim 1.6$). Result models with different gas shock velocity (V_s , in units of km s^{-1}) are plotted with different colours, as indicated. The lines represent the criteria proposed by Kewley et al. (2001) and Pérez-Montero et al. (2013) to separate AGN-like from H II-like objects.

results presented in Table 1 show some major discrepancies for the $[\text{O III}]\lambda 4363/\text{H}\beta$, $([\text{S II}]\lambda 6716, \lambda 6731)/\text{H}\beta$ and $[\text{O I}]\lambda 6300/\text{H}\beta$ line ratios in about half of the observed spectra. The $[\text{O III}]\lambda 4363$ line is strongly blended with the $\text{H}\gamma\lambda 4340$ line, in particular for shock velocities $\geq 100 \text{ km s}^{-1}$. Therefore, the results for the calculated $[\text{O III}]\lambda 4363/\text{H}\beta$ line ratios can differ from the values presenting contamination by the $\text{H}\gamma$ line. Moreover, some of the observed $[\text{S II}]\lambda 6716/\lambda 6731$ line ratios are > 1 , while the calculated ones are < 1 in some objects (Table 1) and for only 57 objects the models were able to reproduce the $[\text{O I}]\lambda 6300/\text{H}\beta$ observational line ratio, with a difference smaller than 50 per cent between the observed and predicted intensities. These problems were explained by Congiu et al. (2017), who pointed out that the contribution of the interstellar medium (ISM) to the extended NLR is particularly high for the $[\text{S II}]$ and $[\text{O I}]$ lines. These lines are emitted by relatively low temperature gas ($T_e \leq 10^4 \text{ K}$). The first ionization potential of sulphur is lower than that of H and the oxygen first ionization potential is similar to that of H. Therefore, these lines can be relatively strong in the ISM as well as those emitted from an ionized-neutral transition zone, located in outskirt layers of the nebulae. Moreover, the $[\text{S III}]\lambda 6312$ line can be blended with the $[\text{O I}]\lambda 6300, \lambda 6363$ doublet, leading to further discrepancies in reproducing the $[\text{O I}]$ lines by the models.

In Fig. 4, a histogram with the distribution of shock velocities V_s (in units of km s^{-1}) predicted by the models for our sample is shown. We find that the clouds in the NLR have V_s ranging from 60 to 310 km s^{-1} , with an average value of $\sim 170 \text{ km s}^{-1}$. For half of the objects (~ 52 per cent) V_s ranges between 200 and 250 km s^{-1} . Moreover, in Fig. 5, the values of some observed line ratios in our sample versus V_s and the resulting polynomial fits of the points, represented by curves, are shown. Most of these line ratios were considered by Dors et al. (2020a) to be used in metallicity estimations of AGNs. The fitting coefficients are listed in Table 3.

The $[\text{O I}]\lambda 6300/\text{H}\alpha$ and $[\text{O III}]\lambda 4363/\text{H}\beta$ line ratios are shown only for the cases in which the models were able to reproduce them, taking into account the uncertainty of 50 per cent.

It can be noticed that:

- (i) the $[\text{O III}]\lambda 5007/\text{H}\beta$ and $[\text{O III}]\lambda 5007/[\text{O II}]\lambda 3727$ line ratios increase with V_s until $\sim 150 \text{ km s}^{-1}$ and decrease for higher velocity values.
- (ii) R_{23} is approximately constant for $V_s \lesssim 150 \text{ km s}^{-1}$ and it decreases for higher velocities.
- (iii) The $[\text{N II}]\lambda 6584/[\text{O II}]\lambda 3727$, $[\text{N II}]\lambda 6584/\text{H}\alpha$, $[\text{O I}]\lambda 6300/\text{H}\alpha$, and $[\text{S II}]\lambda 6725/\text{H}\alpha$ line ratios are approximately constant in the range of the V_s derived values.
- (iv) No conclusions can be obtained from $[\text{O III}]\lambda 4363/\text{H}\beta$ versus V_s due to the small number of points.

It is worth mentioning that, despite the fitting coefficients (see Table 3) indicate that there seems to be a correlation between the line ratios and V_s , the above result is extremely marginal, due to the scattering of the points at a fixed velocity is large. Detailed modelling of a set of lines observed in distinct observational ranges (e.g. optical and ultraviolet) could put more constraints to the models and produce more reliable results, confirming the trend observed in Fig. 5.

The observed behaviour of V_s with the emission-line ratios involving the oxygen lines (e.g. $[\text{O III}]/[\text{O II}]$) is due to the increase of T_e ($\propto V_s^2$) that results in an increase of the intensities of the lines more sensitive to this parameter, i.e. $[\text{O III}]\lambda 5007$ (and eventually oxygen lines from higher ionization levels) rather than $[\text{O II}]\lambda 3727$. However, for $V_s \gtrsim 150 \text{ km s}^{-1}$, the considerable increase of the ionization degree results in an increase of the O^{3+} ion abundance, decreasing the $[\text{O III}]\lambda 5007$ emission. The nitrogen and sulphur lines are less sensitive to V_s . The gas density increases with V_s , therefore the decrease of $[\text{N II}]$, $[\text{O II}]$, and $[\text{S II}]$ lines is mostly due to their relatively low critical density for collisional de-excitation.

One can also note in Figs 4 and 5 that the resulting distribution of velocities V_s in the models is not continuous, with the points being grouped more or less around velocities of 100 and 200 km s^{-1} and few points in between these values. We present an additional analysis in order to explain this results. First, our sample of Seyfert 2 galaxies is rich enough in number of objects to confirm some results obtained for AGNs in general and the result above cannot be associated to the sampling of the models. In Fig. 6, diagrams of our composite model predictions for $[\text{O III}]\lambda 5007/[\text{O II}]\lambda 3727$ line ratios versus flux radiation (F) from the AC and versus the pre-shock density (n_0) are presented in order to understand the role of the main physical parameters. In the left-hand panel of Fig. 6 it can be seen that the galaxies are grouped around $\log F \lesssim 9.3$, $\log F \gtrsim 9.6$ and there seems to be a gap in the range of $9.3 \lesssim \log F \lesssim 9.6$ (F is in units of $\text{ph cm}^{-2} \text{ s}^{-1} \text{ eV}^{-1}$). However, in right-hand panel of Fig. 6, a continuum distribution between $[\text{O III}]/[\text{O II}]$ and n_0 is derived. Another result is shown in Fig. 7, where F is plotted as a function of the shock velocity (left-hand panel) and pre-shock density (right-hand panel). Clearly, it is possible to see few points around $\sim 150 \text{ km s}^{-1}$ confirming the dichotomy and, again, a continuum behaviour of n_0 is found and, obviously, the gap in F is also present. We suggest that objects with $9.3 \lesssim \log F \lesssim 9.6$ or with V_s around $\sim 150 \text{ km s}^{-1}$ could probably correspond to LINERs (see Contini 1997 and references therein), considering that lower velocities would correspond to SF regions and higher velocities to Seyfert galaxies. As LINERs were excluded from our sample due to the criteria adopted by Dors et al. (2020a), this could explain the gap observed in the shock velocities.

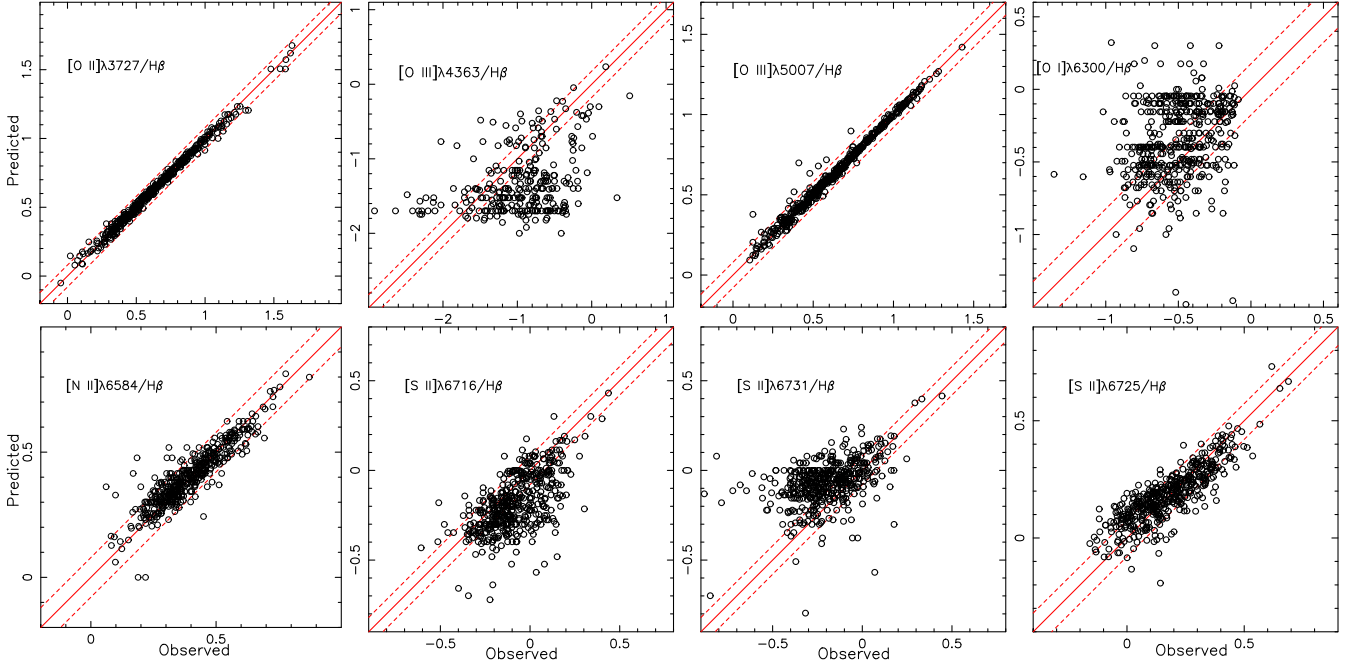


Figure 3. Comparison between the logarithm of model predicted (y-axis) and observed (x-axis) emission-line fluxes relative to the $H\beta$ flux for the sample of 463 Sy2s (see Section 2.1). The solid lines represent the one-to-one relation. The dashed lines show the deviation, representing the observational uncertainty, of the equality by a factor 0.1 and 0.2 dex for strong and weak emission lines, respectively. The line $[S II]\lambda 6725$ corresponds to the sum of the emission-lines $[S II]\lambda 6716$ and $[S II]\lambda 6731$.

Table 2. Model parameters selected to fit the observation emission-line ratios of each object of the sample. Shock velocity V_s in units of km s^{-1} . Atomic pre-shock density n_0 in units of cm^{-3} . Geometrical thickness of the cloud (D) in units of 10^{16} cm . Radiation flux (F) emitted by the AGN (primary source) in units of $10^{10} \text{ photons cm}^{-2} \text{ s}^{-1} \text{ eV}^{-1}$ at the Lyman limit, measured at the inner surface of the cloud. Abundances of N/H, O/H, and S/H are in units of 10^{-4} . The flux of $H\beta$ [$F(H\beta)$] in units of $\text{erg cm}^{-2} \text{ s}^{-1}$ is calculated at the nebula. Full table is available as supplementary material.

Model	V_s	n_0	D	F	N/H	O/H	S/H	$F(H\beta)$
m3	220	260	7.2	1.2	1.0	6.6	0.1	0.071
m4	240	300	9.2	2.0	1.2	6.6	0.2	0.180

Concerning the results for the element abundances of our sample, the models predict oxygen abundances in the range $8.5 \lesssim [12 + \log(O/H)] \lesssim 8.9$, with an average value of 8.8 ± 0.03 . Adopting the solar value $12 + \log(O/H)_\odot = 8.89$ (Alende Prieto, Lambert & Asplund 2001), the O/H values above correspond to the metallicity range $0.6 \lesssim (Z/Z_\odot) \lesssim 1.6$, and an average value $(Z/Z_\odot) \approx 1.3$. The logarithm of the N/O abundance ratio is in the range $-1.1 \lesssim [\log(N/O)] \lesssim -0.3$ with an average value -0.8 ± 0.12 .

4 DISCUSSION

Shocks created by the interaction of radio jets/outflows with the surrounding ISM, in addition to photoionization by radiation from the accretion disc, have a strong influence on the observed emission lines of AGNs. Observations carried out along decades have shown that outflows are commonly observed in AGNs (for a review see e.g. King & Pounds 2015; Harrison et al. 2018). In the early years, outflows were observed mainly in powerful radio galaxies as, for instance, in 3C 405 (Cygnus A) by Tadhunter (1991), showing velocities around 1800 km s^{-1} and recent studies have shown that around 40 percent of the quasars present outflows (see Arav et al. 2020 and

references therein). Concerning lower luminosity AGNs, such as Seyferts, outflows have also been observed, but with relatively lower velocities. For example, May et al. (2018) found ionized outflows with velocities of $\sim 700 \text{ km s}^{-1}$ in the central 170 pc of the nearby Seyfert nucleus ESO 428-G14. Using the data from the MaNGA survey (Blanton, Bershady & Abolfathi B. et al. 2017), Ilha, Riffer & Schimoia J. et al. (2019) studied the gas kinematics of a sample of 62 Seyferts and LINERs. By comparing their AGN sample with a sample of non-active galaxies (see also e.g. Riffer et al. 2020; Wylezalek et al. 2020) they found that outflow signatures in the ionized gas within the central 1–2 kpc with velocity $v < 400 \text{ km s}^{-1}$ are seen in most AGN hosts.

From a theoretical point of view, pure shock models (e.g. Binette, Dopita & Tuohy 1985; Dopita & Sutherland 1996; Allen et al. 2008; Alarie & Morisset 2019) and composite models (shock+AGN, e.g. Contini & Aldrovandi 1983, 1986; Congiu et al. 2017; Contini 2017, 2019) have predicted shock velocities in Seyfert NLR between 100 and 500 km s^{-1} . From the detailed modelling of the present large sample of Seyfert 2, we derived a similar range of shock velocities (from 60 to 310 km s^{-1}) to those obtained in previous works. Moreover, this range of velocities is in agreement with those

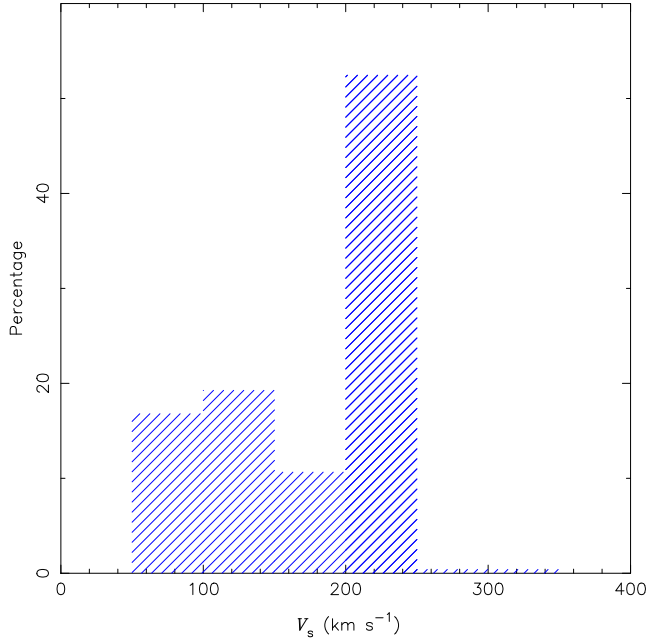


Figure 4. Distribution of shock of the velocities V_s predicted by the composite models (see Section 2.2) for our sample, in velocity bins of 50 km s^{-1} .

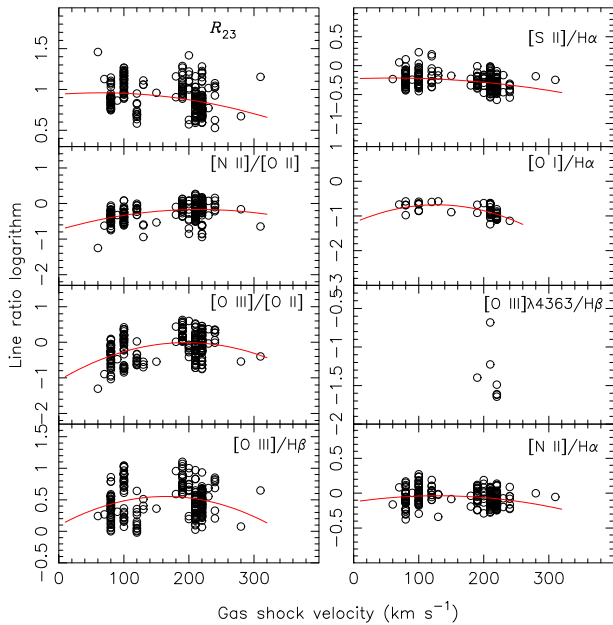


Figure 5. Observed line ratios of the sample objects (see Section 2.1) versus the gas shock velocity predicted by the models (see Section 2.2). In each panel the related line ratio is indicated. Curves represent the fit of a second order polynomial whose coefficients are listed in Table 3.

found in observational investigations of Seyfert 2 NLR, strengthening the confidence in our results. The present modelling of the spectra, which makes use of a large range of physical parameters, offers a unique opportunity to investigate several properties of Seyfert galaxies, such as their position in diagnostic diagrams as a function of different shock parameters, the temperature, and ionization structure and chemical abundance determinations. Each of these issues is discussed in the following.

4.1 Diagnostic diagrams

Baldwin et al. (1981) proposed that a combination of two pairs of line ratios, originally $[\text{O III}]\lambda 5007/\text{H}\beta$ versus $[\text{N II}]\lambda 6584/\text{H}\alpha$, can be used to discriminate the ionizing source of line emitting objects, i.e. objects ionized by hot stars and by a non-thermal source. These and other combinations of line ratios are known as the BPT diagrams (see also Veilleux & Osterbrock 1987; Kewley et al. 2001, 2013; Kauffmann et al. 2003; Pérez-Montero et al. 2013; Ji & Yan 2020). In particular, the sequence formed by AGN emission-line ratios in BPT diagrams has been explained by variations in the physical parameters according to different assumptions (e.g. Ji et al. 2020).

(i) Pure photoionization: considering photoionization of AGN clouds by radiation from gas accretion into a black hole, whose SED can be represented by a power law. For example, Feltre et al. (2016) showed that the increase of certain line ratios, such as $[\text{O III}]\lambda 5007/\text{H}\beta$, is mainly due to the combination of metallicity with the ionization parameter (see also Groves et al. 2006). A secondary dependence between the hardness of the SED and the electron density with the line ratios is also found (e.g. Feltre et al. 2016; Carvalho et al. 2020).

(ii) Simple equilibrium model: Flury & Moran (2020), assuming an approach for estimating abundances of heavy elements, which involves a reverse-engineering of the direct method,⁴ showed that high $[\text{O III}]\lambda 5007/\text{H}\beta$ and $[\text{N II}]\lambda 6584/\text{H}\alpha$ values are associated to high O/H and ionization degree values of the gas phase.

(iii) Pure shock heating and ionization effects: Dopita & Sutherland (1995), by using radiative steady-flow shock models (Dopita & Sutherland 1996), showed that, at a fixed solar metallicity, most of the line ratios involved in the BPT diagrams increase with V_s (see also Allen et al. 2008).

(iv) Starburst-AGN mixing: Davies et al. (2014a, b), who combined stellar evolutionary synthesis models from the STARBURST99 code (Leitherer et al. 1999) with the MAPPINGS photoionization code (Binette et al. 1985), showed that for spatially resolved objects, hence the metallicity and the ionization parameters are fixed, the increase of some line ratios in BPT diagrams can be interpreted in terms of the ionization flux fraction of SFs to AGN. AGNs with the highest line intensity ratios have less SF flux contamination. Thomas et al. (2018) also considered a Starburst-AGN mixing to interpret SDSS data of AGNs and found that, even for strong AGNs [with $\log([\text{O III}]\lambda 5007/\text{H}\beta) \gtrsim 0.9$], ~ 30 per cent of the Balmer line flux on average comes from H II regions.

Our sample is based on integrated SDSS spectra taken with a fixed optical fibre diameter of ~ 3 arcsec, which corresponds to a physical scale (D) at the galaxies in the range $1.8 \lesssim D(\text{kpc}) \lesssim 15$. Although an H II region contribution is expected (Thomas et al. 2018), the emission from the sample galaxies is mainly from the AGN. In fact, Dors et al. (2020a) did not find any correlation between the oxygen abundance and the electron density of AGNs with the redshift, indicating that the aperture effect does not affect the derived parameters of the SDSS sample, at least for $z \lesssim 0.4$ (see also Kewley, Jansen & Geller 2005). As an additional test, in Fig. 8, the shock velocity derived from modelling is plotted against the redshift value of each object of our sample. Since the contribution of H II region fluxes to the AGN tends to increase with the distance from the nuclei (Davies et al. 2014a, b) and, in general, SFs show

⁴Direct method or T_e -method is based on elemental abundance of heavy elements calculated by using direct estimations of the electron temperature and electron density.

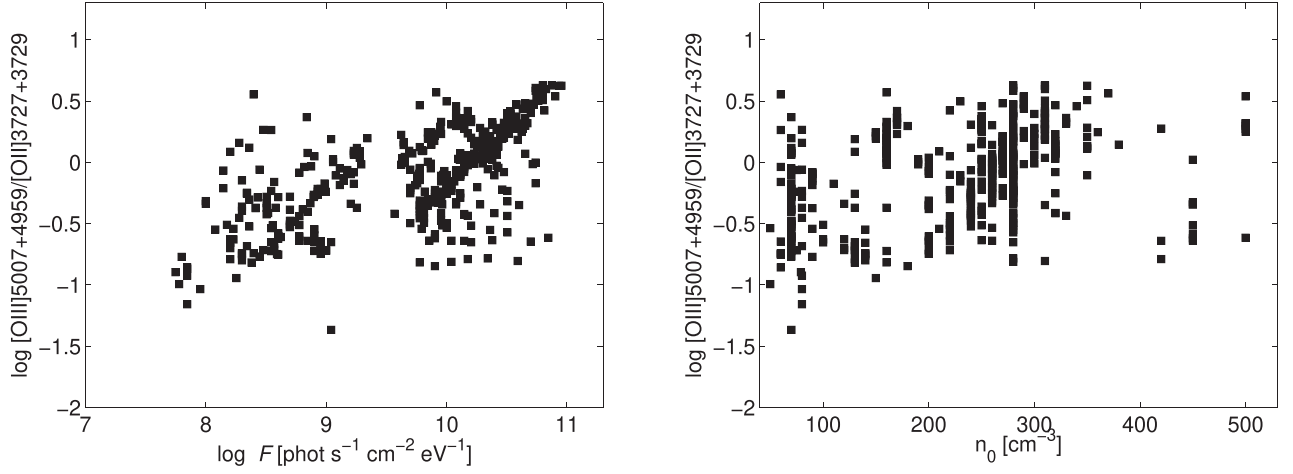


Figure 6. Diagrams of $[\text{O III}](\lambda 5007 + \lambda 4959)/[\text{O II}]\lambda 3727$ intensity ratios versus the logarithm of the flux radiation ($\log F$) from the AC (left-hand panel) and pre-shock density (n_0 , right-hand panel).

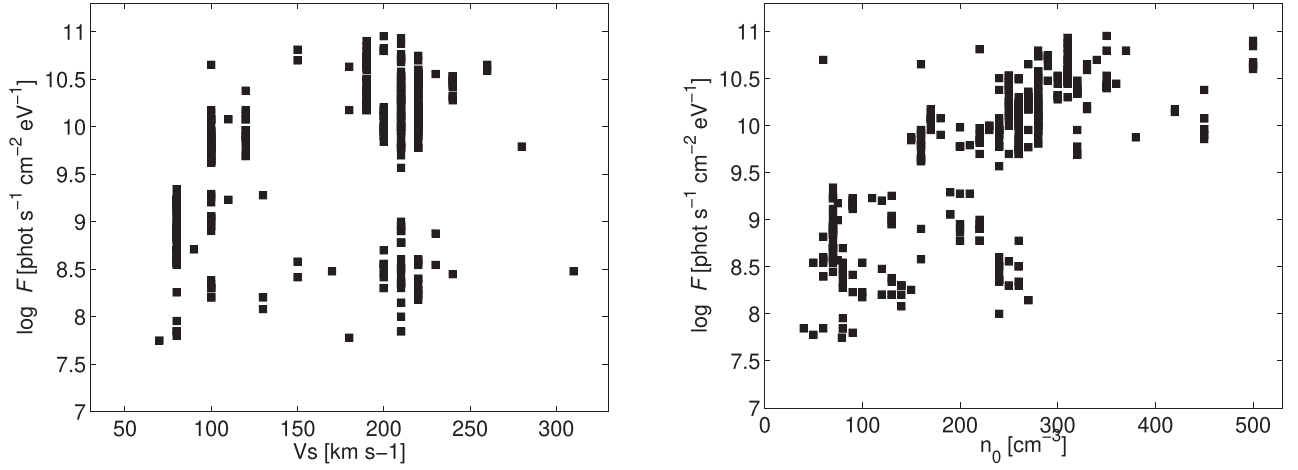


Figure 7. Logarithm of the flux radiation $\log F$ from the AC versus the shock velocity (V_s , left-hand panel) and versus the pre-shock density (n_0 , right-hand panel).

Table 3. Coefficients of the fitting of $R = aV_s^2 + bV_s + c$ to the points shown in Fig. 3. R correspond to different line ratios as indicated.

R	$a (\times 10^{-5})$	$b (\times 10^{-3})$	c
$[\text{O III}]/\text{H}\beta$	$-1.72 (\pm 0.75)$	$5.64 (\pm 2.35)$	$+0.09 (\pm 0.16)$
$[\text{O III}]/[\text{O II}]$	$-2.76 (\pm 1.00)$	$10.82 (\pm 3.15)$	$-1.07 (\pm 0.21)$
$[\text{N II}]/[\text{O II}]$	$-1.23 (\pm 0.65)$	$5.30 (\pm 2.03)$	$-0.74 (\pm 0.14)$
R_{23}	$-0.46 (\pm 0.51)$	$0.59 (\pm 1.59)$	$+0.94 (\pm 0.10)$
$[\text{N II}]/\text{H}\alpha$	$-0.52 (\pm 0.33)$	$1.36 (\pm 1.04)$	$-0.12 (\pm 0.07)$
$[\text{O I}]/\text{H}\alpha$	$-3.20 (\pm 1.25)$	$8.17 (\pm 3.86)$	$+1.05 (\pm 0.10)$
$[\text{S II}]/\text{H}\alpha$	$-0.36 (\pm 0.36)$	$0.42 (\pm 1.13)$	$-0.12 (\pm 0.07)$

low shock velocities, a decrease of V_s with z would be expected if a significant fraction of the nuclear emission of the galaxies of our sample can be attributed to the contamination from extra-nuclear H II regions. However, Fig. 8 shows no correlation between V_s and the redshift. Therefore, we conclude that the SFs flux contribution to the AGN spectra of our sample is negligible and, consequently, the derived parameters based on the composite models are not affected by it.

In Fig. 9, we verify the position of our sample objects in the $[\text{O III}]\lambda 5007/\text{H}\beta$ versus $[\text{N II}]\lambda 6584/\text{H}\alpha$ diagnostic diagram in terms of the abundance ratios $12+\log(\text{O}/\text{H})$ (left-hand panel). In disagreement with pure photoionization model results (e.g. Feltre et al. 2016), it is not possible to distinguish objects with different O/H values in this diagram. Our models predict a narrow range (see above) of O/H abundances and the large majority of our sample objects (~ 99 per cent) shows $12+\log(\text{O}/\text{H})$ values higher than 8.7 dex. A narrow metallicity range for AGNs, with $12+\log(\text{O}/\text{H})$ varying by ~ 0.1 dex as a function of host galaxy stellar mass over the range $10.1 \lesssim \log(M/M_\odot) \lesssim 11.3$, was also derived by Thomas et al. (2019), who used the Bayesian parameter estimation code NEBULABAYES. The derived narrow O/H range by the composite models for our sample reflects a stronger dependence of oxygen emission lines on shock parameters (e.g. V_s) rather than the O/H abundance. Moreover, there is a degeneracy in the models which is also found in pure photoionization models. In fact, Davies et al. (2014b) who considered the Starburst-AGN mixing models, pointed out that metallicity and ionization parameters are degenerated quantities because pure photoionization models adopting different combinations of these parameters can produce similar line ratios.

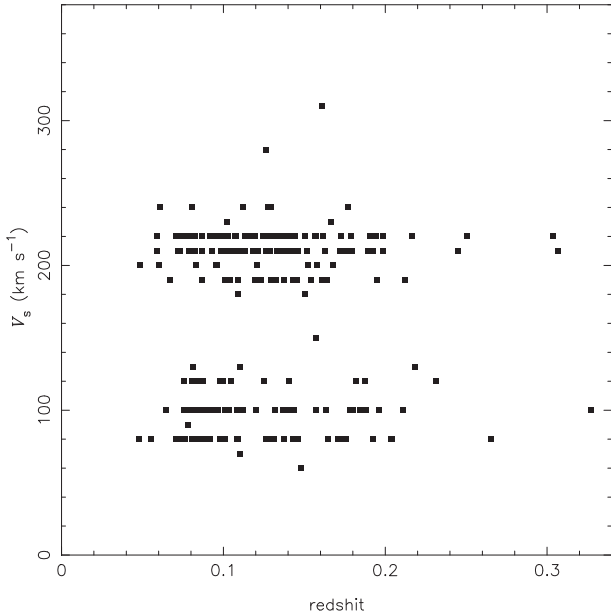


Figure 8. Shock velocity V_s predicted by the composite models versus the redshift for the sample objects.

In our case, models adopting different V_s , n_0 , and metallicities can produce similar emission-line intensities. The degeneracy disappears when many lines from different ionization levels are observed for each element in single spectra.

The right-hand panel of Fig. 9 shows the BPT diagram for our sample in terms of different N/O abundance values, represented by the different colours of the points. There is a clear trend showing that objects with higher $\log(\text{N/O})$ have also higher $[\text{N II}]\lambda 6584/\text{H}\alpha$ values. Although expected (see Ji et al. 2020), this result is very interesting, because the interpretations of observation data of AGNs based on shock models, in general, consider a fixed value for the metallicity (or oxygen abundance). Moreover, this result indicates that our composite models are able to estimate N/O abundances by using nitrogen lines, less sensitive to V_s . Other diagnostic diagrams involving $[\text{O I}]\lambda 6300/\text{H}\alpha$ and $[\text{S II}]\lambda 6725/\text{H}\alpha$ are not considered as these line ratios show a low dependence with O/H and N/O abundance ratios.

In Fig. 10, three diagnostic diagrams, $[\text{O III}]\lambda 5007/\text{H}\beta$ versus $[\text{N II}]\lambda 6584/\text{H}\alpha$, $[\text{O I}]\lambda 6300/\text{H}\alpha$ and $[\text{S II}]\lambda 6725/\text{H}\alpha$, the objects of our sample are separated according to the predicted composite model results for the shock velocity V_s . There is no correlation between the position of the objects and V_s . The highest values of $[\text{O III}]\lambda 5007/\text{H}\beta$ correspond to V_s in the range 100–200 km s^{−1}. This is due, for models with $V_s \gtrsim 200$ km s^{−1}, to the O^{3+} ionic abundance increase and, consequently, to the decrease of the lines emitted by O^{2+} ion, as already reported above. One direct consequence of this result is that standard diagnostic diagrams, based on integrated spectra, cannot be used to distinguish the shock velocities in AGNs.

Another important issue is to investigate the positions in the BPT diagrams of the objects whose dominant ionization mechanism is shock and to compare their position with that of photoionized objects. As previously reported, AGNs with $F < 10^9$ ph cm^{−2} s^{−1} eV^{−1} are considered as being shock-dominated, otherwise they are considered as being photoionization-dominated. The shock-dominated regime is characterized by $\log([\text{O III}]\lambda 5007/[\text{O II}]\lambda 3727) \lesssim 0$, as pointed out by Contini (2012), who used composite models to reproduce the continuum and optical lines emitted from the extended narrow-

line region (ENLR) of the Seyfert 2 galaxy NGC 7212. In Fig. 11, we show the logarithm of the line ratios $[\text{O III}]\lambda 5007/[\text{O II}]\lambda 3727$ versus $[\text{N II}]\lambda 6584/\text{H}\alpha$, $[\text{O I}]\lambda 6300/\text{H}\alpha$, and $[\text{S II}]\lambda 6725/\text{H}\alpha$ for our sample, splitted in terms of shock-dominated and photoionization-dominated. Although an overlap of the line ratios from the different regimes can be seen, the highest and the lowest $[\text{O III}]/[\text{O II}]$ are only observed in photoionization and shock-dominated objects, respectively. In Fig. 12, the shock- and photoionization-dominated objects of our sample are plotted in the BPT diagrams. Although there is some overlap, photoionization-dominated models present higher $[\text{O III}]/\text{H}\beta$ values while the shock-dominated models present lower values.

4.2 Chemical abundances

The heavy element abundances in Seyfert 2 have been obtained in general only for oxygen and adopting pure photoionization models. In fact, Ferland & Netzer (1983), by using the first versions of the CLOUDY code (Ferland & Truran 1980), showed that models employing a power-law ionizing continuum, metallicities in the range $0.1 \leq (Z/Z_\odot) \leq 1.0$ and ionization parameter in the range $-4.0 \leq (\log U) \leq -2.0$ are able to describe the sequence of the optical emission-line ratios of Seyferts in BPT diagrams. After this pioneering work many authors have invoked pure photoionization models to derive physical properties of AGN NLRs at low (e.g. Stasińska 1984; Ferland & Osterbrock 1986; Cruz-Gonzalez et al. 1991; Storchi-Bergmann et al. 1998; Groves et al. 2006; Feltre et al. 2016; Castro et al. 2017; Pérez-Montero et al. 2019; Carvalho et al. 2020) and high redshifts (e.g. Nagao et al. 2006; Matsuoka et al. 2009, 2018; Dors et al. 2018; Nakajima et al. 2018; Mignoli et al. 2019; Guo et al. 2020). Dors et al. (2020a) showed that the methods based on pure photoionization models derive $12+\log(\text{O/H})$ values in the range from ~ 7.2 to ~ 9.2 . Among the methods considered by Dors et al. (2020a), the results obtained through the H II-CHI-MISTRY code (Pérez-Montero 2014) can be used to compare abundances obtained adopting pure photoionization with those based on composite models. The H II-CHI-MISTRY code was adapted for AGNs by Pérez-Montero et al. (2019) and establishes a Bayesian-like comparison between predictions from a grid of photoionization models, built with the CLOUDY code (Ferland et al. 2017), and observational emission-line ratios. In view of this, in Fig. 13, the N/O versus O/H abundance values derived from H II-CHI-MISTRY code by Pérez-Montero et al. (2019) for the 244 objects of our sample are compared with those derived by our composite models. In addition, in Fig. 13, the values predicted by individual photoionization models for a different sample of 47 Seyfert 2 nuclei ($z < 0.1$) by Dors et al. (2017), obtained by the CLOUDY code, and estimates for H II regions derived by Pilyugin & Grebel (2016), who adopted the C method (Pilyugin, Grebel & Mattsson 2012), are shown. Despite the scattering, the abundance results based on the composite models and those from the H II-CHI-MISTRY code are located in the same region in Fig. 13. However, the former predicts a narrower range of O/H values than those from the latter. As can be seen in the Fig. 13, the points of the sample from Dors et al. (2017) occupy the region of highest metallicity, which is probably due to the fact that the sample considered in that work is different from the one considered here, consisting mostly of strong AGNs, i.e. with very high $[\text{O III}]\lambda 5007/\text{H}\beta$ ratios (see fig. 1 of Dors et al. 2020b).

The difference between the O/H abundance results obtained by SUMA and those obtained by CLOUDY, i.e. by the H II-CHI-MISTRY code, is due to the presence of shocks in our models, explained as follows. In case of ejection, the clouds move outwards. The shock

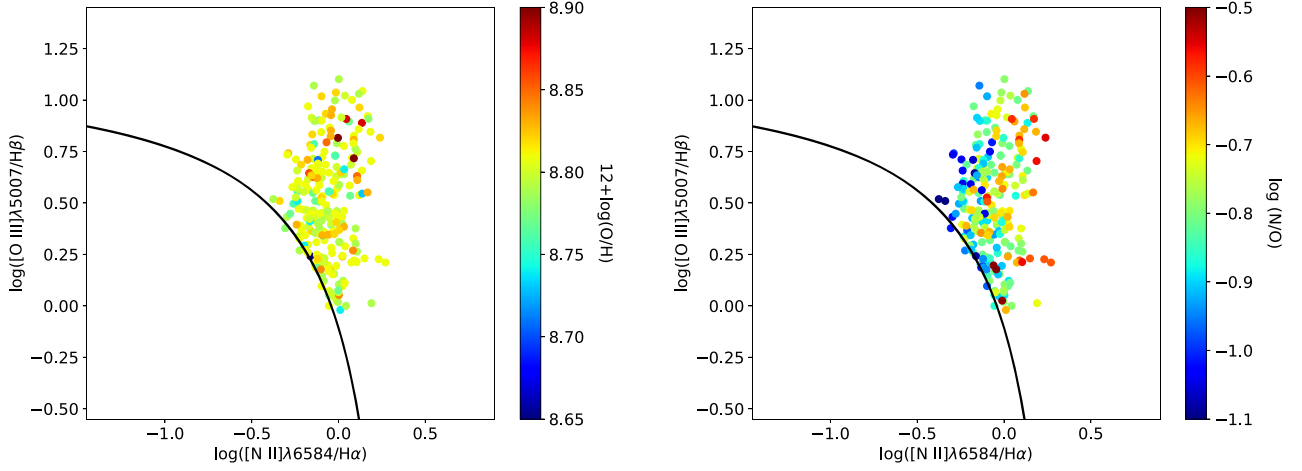


Figure 9. Diagnostic diagram $[\text{O III}]\lambda 5007/\text{H}\beta$ versus $[\text{N II}]\lambda 6584/\text{H}\alpha$. The points represent objects of our sample and the colour bars show the predicted composite model values of $12+\log(\text{O}/\text{H})$ (left-hand panel) and $\log(\text{N}/\text{O})$ (right-hand panel) abundance ratios. Line represents the criterion proposed by Kewley et al. (2001) to separate AGN-like and H II-like objects.

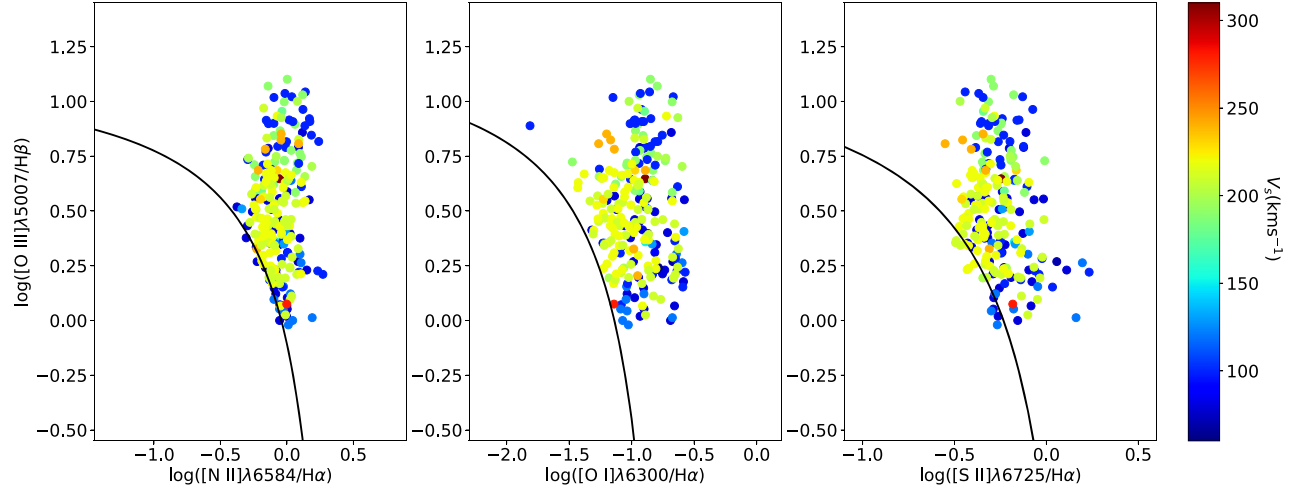


Figure 10. Diagnostic diagrams $[\text{O III}]\lambda 5007/\text{H}\beta$ versus $[\text{N II}]\lambda 6584/\text{H}\alpha$, versus $[\text{O I}]\lambda 6300/\text{H}\alpha$ and versus $[\text{S II}]\lambda 6725/\text{H}\alpha$. The points represent objects of our sample (see Section 2.1) separated according to the shock velocities (V_s in units of km s^{-1}) predicted by our composite models. The lines represent the criteria proposed by Kewley et al. (2001) and Pérez-Montero et al. (2013) to separate AGN-like from H II-like objects.

front is on the outer edge of the clouds, while the photoionization flux from AC reaches the opposite (internal) edge. Therefore different temperature profile and ionization structure throughout the clouds are predicted by the SUMA and CLOUDY codes and, consequently, different O/H abundances result because the oxygen lines are strongly dependent on the shock parameters. To illustrate this point, we select from our results two models; one predicted to be shock dominated (m6) and another one which is photoionization dominated (m26). The set of parameters $[12+\log(\text{O}/\text{H}), V_s (\text{km s}^{-1}), n_0 (\text{cm}^{-3}), \log F]$ for m6 and m26 are (8.81, 150, 90, 8.41) and (8.81, 100, 160, 9.95), respectively (see Table 2). The CLOUDY models were obtained by Pérez-Montero et al. (2019) and the set of parameters $[12+\log(\text{O}/\text{H}), N_e (\text{cm}^{-3}), \alpha_{\text{ox}}, \log U]$ for m6 and m26 are [8.82, 500, -0.8, -2.0] and [8.77, 500, -0.8, -2.1], respectively. In Fig. 14, we illustrate the profiles of T_e and of the fractional abundances of the oxygen ions O^+/O and O^{2+}/O throughout the clouds of m6 and m26 in order to understand the $[\text{O II}]$ and $[\text{O III}]$

line intensity results. The distance R from the edge illuminated by the AC radiation within the cloud was normalized by the outermost radius R_e of each model. In order to clarify the figure interpretation, the radiation illuminated and the shock front (for the SUMA models) positions are indicated in Fig. 14. For both SUMA results, one can see that T_e reaches a high value ($T_e \sim 10^5 \text{ K}$) downstream near the shock front. However, for the photoionization dominated model, T_e reaches about the same value predicted by the CLOUDY model at $(R/R_e) \lesssim 0.9$. Otherwise, for the shock dominated model, high T_e values extend to about half of the radius. Concerning the O^+/O fractional abundance, both photoionization and shock-dominated models produce different profiles to those calculated by the CLOUDY, with the shock-dominated model producing very small fractional abundance for $(R/R_e) \gtrsim 0.6$. Finally, O^{2+}/O structures predicted by both SUMA models indicate a higher level of ionization along the radius as compared to those calculated by the CLOUDY models, being more pronounced for the shock-dominated model.

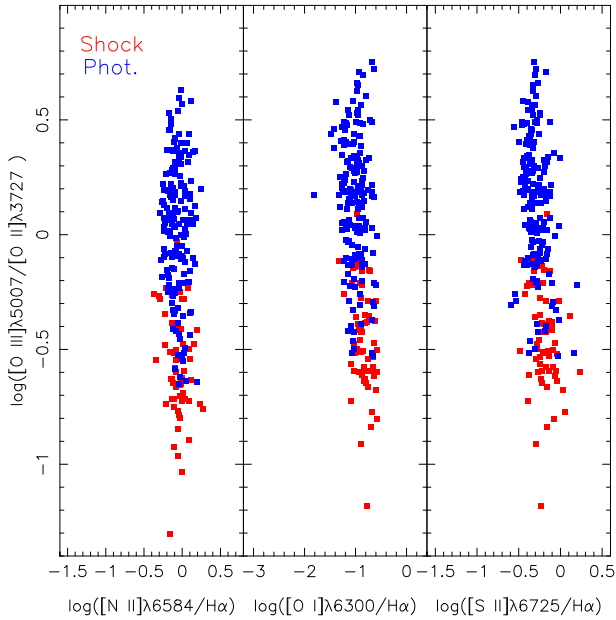


Figure 11. Logarithm of the line ratios $[\text{O III}]\lambda 5007/[\text{O II}]\lambda 3727$ versus $[\text{N II}]\lambda 6584/\text{H}\alpha$, $[\text{O I}]\lambda 6300/\text{H}\alpha$ and $[\text{S II}]\lambda 6725/\text{H}\alpha$. The red and blue points represent objects of our sample classified as shock ($F < 10^9 \text{ ph cm}^{-2} \text{ s}^{-1} \text{ eV}^{-1}$) and photoionization dominated, respectively.

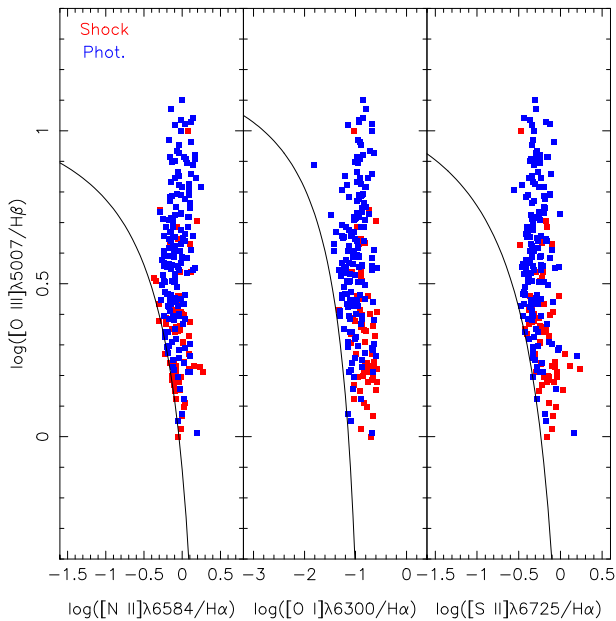


Figure 12. As Fig. 11 but for the logarithm of the line ratios $[\text{O III}]\lambda 5007/\text{H}\beta$ versus $[\text{N II}]\lambda 6584/\text{H}\alpha$, $[\text{O I}]\lambda 6300/\text{H}\alpha$ and $[\text{S II}]\lambda 6725/\text{H}\alpha$.

Therefore, any physical property derived through $[\text{O II}]$, $[\text{O III}]$, and high ionization lines (e.g. $[\text{Fe VII}]\lambda 6087$, $[\text{Fe X}]\lambda 6375$, etc.) can be very different when composite or pure photoionization models are adopted.

4.3 Abundance calibrations

Storchi-Bergmann et al. (1998) proposed the first calibration between the metallicity (in terms of O/H) and narrow optical emission line ratios of AGNs. After this pioneering work, Castro et al. (2017)

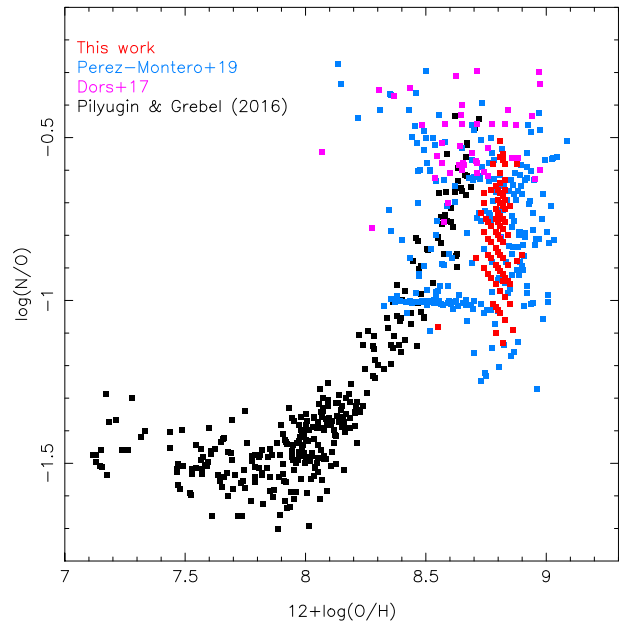


Figure 13. $\log(\text{N}/\text{O})$ versus $12 + \log(\text{O}/\text{H})$ abundance ratio values. The red points are values predicted by the COMPOSITE models (see Section 2.2). The blue points are predicted values obtained by Pérez-Montero et al. (2019) using the H II-CHI-MISTRY code for the same sample of objects considered in this work. The pink points represent values predicted by detailed photoionization models for a sample of 47 Seyfert 2 nuclei ($z < 0.1$) by Dors et al. (2017). The black points are estimations for H II regions derived by Pilyugin & Grebel (2016) adopting the C method (Pilyugin et al. 2012).

and Carvalho et al. (2020) proposed semi-empirical calibrations based on the line ratios $\text{N}_2\text{O}_2 = \log(\text{N II}\lambda 6584/\text{O II}\lambda 3727)$ and $\text{N}_2 = \log(\text{N II}\lambda 6584/\text{H}\alpha)$, respectively. In particular, Castro et al. (2017) pointed out the importance of considering emission lines emitted by ions with similar ionization potential, in order to minimize the shock effects on calibrations. In fact, as shown in Fig. 14, the inclusion of shocks in the gas ionization rate, in addition to photoionization from AGN, produces different temperature and fractional abundance profiles, mainly for shock-dominated objects. In this sense, the N_2O_2 index has an advantage relative to other line ratios because the involved ions, N^+ and O^+ , have close ionization potentials, i.e. 29.60 and 35.12 eV, respectively.

All calibrations between Z and strong emission lines for AGNs available in the literature (for a review, see Dors et al. 2020a) are based on pure photoionization models and it is thus worth to obtain new calibrations considering the contribution from shocks to the NLR. Therefore, in Fig. 15, the predicted N/O abundance ratio versus the observational N_2O_2 value for each object of our sample is shown. A clear correlation can be seen between the points (with the Pearson correlation coefficient equal to 0.65) and it is represented by

$$\log(\text{N}/\text{O}) = (0.51 \pm 0.02) \times \text{N}_2\text{O}_2 + (-0.68 \pm 0.01). \quad (1)$$

Similarly, a $(\text{N}/\text{O})-\text{N}_2\text{O}_2$ calibration was proposed by Pérez-Montero & Contini (2009) for H II regions.

Considering that this is the first metallicity calibration derived using composite models, a comparison with calibrations proposed by other authors should be presented. The unique calibration which uses the N_2O_2 index as metallicity indicator for AGNs has been proposed by Castro et al. (2017),

$$(Z/Z_\odot) = 1.08 \times \text{N}_2\text{O}_2^2 + 1.78 \times \text{N}_2\text{O}_2 + 1.24. \quad (2)$$

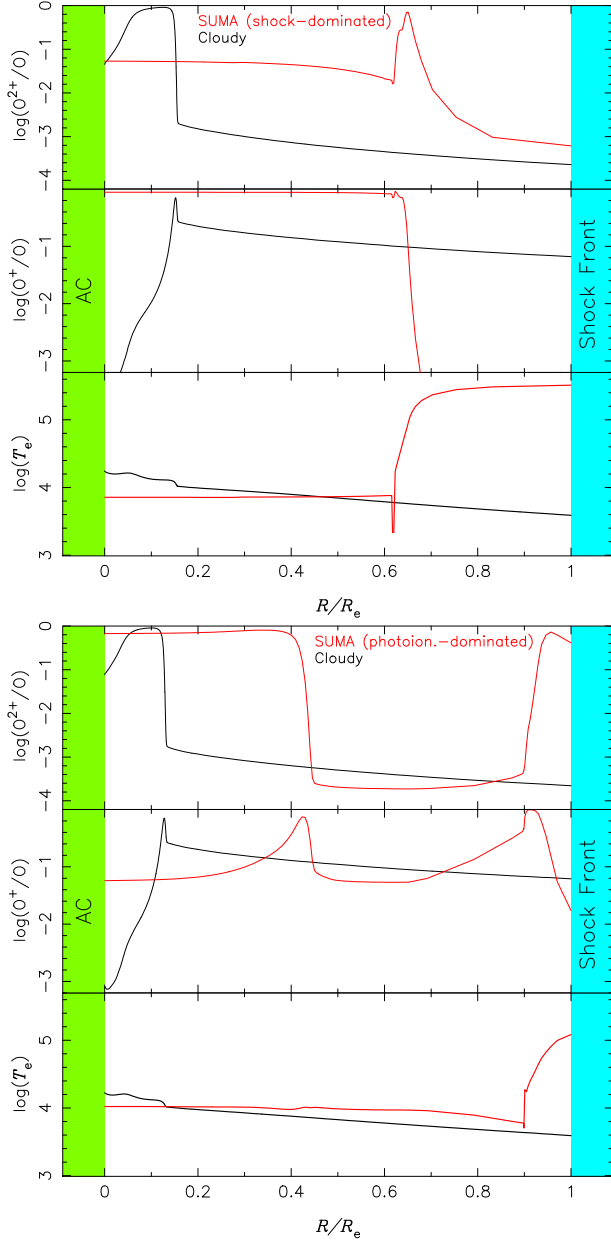


Figure 14. Profiles of electron temperature (T_e) and fractional abundances of the oxygen ions O^+/O and O^{2+}/O predicted by SUMA and CLOUDY codes. The distance R from the edge reached by radiation from active centre (AC) was normalized by the outermost radius R_e of each model. The positions of the edge illuminated by the AC radiation and of the shock front (for SUMA models) are indicated in each plot. Top panel: Profiles for a shock dominated model (m6). The parameter set [$12+\log(O/H)$, V_s (km s $^{-1}$), n_0 (cm $^{-3}$), $\log F$] for the SUMA model are (8.81, 150, 90, 8.41). The CLOUDY model was obtained from Pérez-Montero et al. (2019) assuming the parameter set [$12+\log(O/H)$, N_e (cm $^{-3}$), $\alpha_o x$, $\log U$] equal to [8.82, 500, -0.8 , -2.0]. Bottom panel: As the top panel but for a photoionization dominated model (m26) with SUMA and CLOUDY parameters (8.81, 100, 160, 9.95) and [8.77, 500, -0.8 , -2.1], respectively.

Nevertheless, this calibration considers the metallicity and our calibration the relative abundance N/O ($\sim Z$; Vila-Costas & Edmunds 1993; Henry, Edmunds & Köppen 2000). Therefore, to consistently compare both calibrations the following procedure is carry out. First,

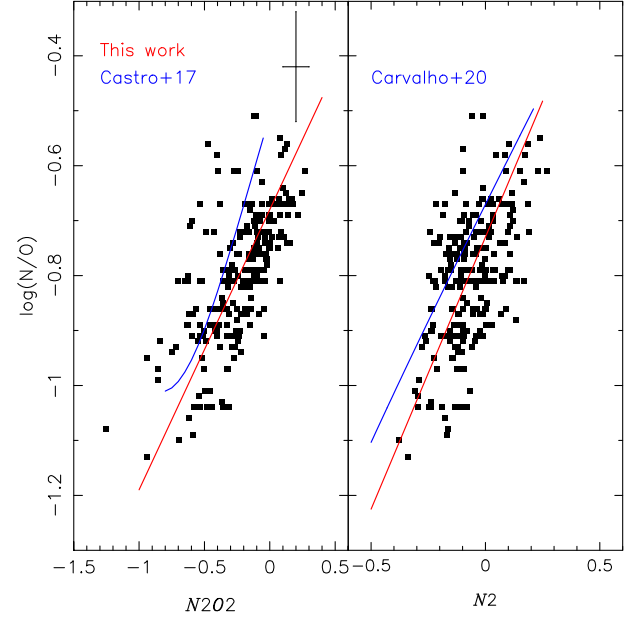


Figure 15. Left-hand panel: Logarithm of the abundance ratio N/O versus $N_2O_2 = \log(N \Pi \lambda 6584 / O \Pi \lambda 3727)$. Points represent the $\log(N/O)$ predicted by the composite models (see Section 2.2) and the corresponding observational N_2O_2 of the sample objects (see Section 2.1). The red line represents the linear fit to the points given by equation (1). The blue line represents the $(N/O)-N_2O_2$ derived by using the calibration proposed by Castro et al. (2017) (equations 2, 3, and 4). Error bars represent the observational error of N_2O_2 and the uncertainty in the estimation of $\log(N/O)$ (e.g. Denicoló et al. 2020). Right-hand panel: Same as left-hand panel but for $\log(N/O)$ versus N_2 . The red line represents the linear fitting to the points given by equation (5). The blue line represents the $(N/O)-N_2O_2$ derived by using the calibration proposed by Carvalho et al. (2020) (equation 6) and equations (3) and (4).

we convert the (Z/Z_\odot) values in O/H abundances assuming

$$12 + \log(O/H) = 12 + \log[(Z/Z_\odot) \times 10^{\log(O/H)_\odot}], \quad (3)$$

where $\log(O/H)_\odot = -3.31$ (Alende Prieto et al. 2001). Then, we take into account the $(N/O)-(O/H)$ relation derived by Dors et al. (2017), obtained by using abundance estimates of H II regions and Seyfert 2, given by

$$\log(N/O) = 1.29 \times 12 + \log(O/H) - 11.84. \quad (4)$$

The resulting $(N/O)-(N_2O_2)$ Castro et al. (2017) calibration is compared to our calibration (equation 1) in Fig. 15, left-hand panel, where a good agreement can be observed, taking into account the observational error of N_2O_2 (~ 0.1 dex) and the uncertainty of ~ 0.2 dex in estimations based on strong-line methods (e.g. Denicoló, Terlevich & Terlevich 2020).

Taking into account that the N_2O_2 parameter could be affected by reddening correction, we also explore the relation with N_2 parameter that is not affected by reddening correction. In Fig. 15, right-hand panel, we present the linear calibration between $\log(N/O)$ and N_2 , obtaining

$$\log(N/O) = (0.99 \pm 0.05) \times N_2 + (-0.73 \pm 0.01), \quad (5)$$

with the Pearson correlation coefficient equal to 0.55. Carvalho et al. (2020) proposed a semi-empirical calibration, based on the CLOUDY models, between Z and N_2 given by

$$(Z/Z_\odot) = 4.01^{N_2} - 0.07. \quad (6)$$

We adopt the same procedure previously described to convert the metallicity values derived from the calibration by Carvalho et al. (2020) into N/O and obtain a calibration between this abundance ratio and N_2 . The resulting calibration is compared with the one obtained through the composite models (equation 5) in Fig. 15, right-hand panel. As in the case of the $(N/O)-(N_2O_2)$, both calibrations are in agreement each other taking into account the uncertainties in estimates based on strong-line methods. Since the dispersion present in both panels are very similar, we can conclude that the N_2O_2 relation proposed in this work is not strongly affected by reddening correction.

5 CONCLUSION REMARKS

In this work, by using the SUMA code, we calculate the photoionization and shock parameters suitable to reproduce the optical ($3000 < \lambda(\text{\AA}) < 7000$) emission lines emitted from the NLRs of 244 Seyfert 2 nuclei in the local universe ($z \lesssim 0.4$). The observation data were taken from the SDSS. Based on the results of the detailed modelling, we found that Seyfert 2 present shocks in their NLRs with velocities in the range ~ 50 to $\sim 300 \text{ km s}^{-1}$ and an average value $\sim 170 \text{ km s}^{-1}$. A narrower range of metallicities ($0.6 \lesssim (Z/Z_\odot) \lesssim 1.6$) than that estimated from pure photoionization models is derived for the sample. The standard diagnostic diagrams $[O III]\lambda 5007/H\beta$ versus $[N II]\lambda 6584/H\alpha$, $[O I]\lambda 6300/H\alpha$ and $[S II]\lambda 6725/H\alpha$, based on integrated spectra, can be used to discriminate between shock and photoionization dominated objects. However, our results indicate that shock velocity in AGNs cannot be estimated by these standard optical line ratio diagrams. Also, our results show that the temperature structure and O^+/O and O^{2+}/O fractional abundance profiles along the radius of the emitting nebula are highly modified by the shock presence. These results suggest that a combination of lines emitted by ions with similar ionization potential, in order to minimize the shock effects, are preferable to other metallicity indicators. Finally, from our model results it was possible to derive calibrations between the N/O abundance ratio and the $N_2O_2 = \log(N II \lambda 6584/O II \lambda 3727)$ and $N_2 = \log(N II \lambda 6584/H\alpha)$ indexes. These calibrations are in agreement with those derived from pure photoionization models.

ACKNOWLEDGEMENTS

We are grateful to the referee for his/her dedicated work in reviewing our paper. OLD and ACK are grateful to Fundação de Amparo à Pesquisa do Estado de São Paulo (FAPESP) and Conselho Nacional de Desenvolvimento Científico e Tecnológico (CNPq). RAR thanks partial financial support from Fundação de Amparo à Pesquisa do Estado do Rio Grande do Sul (17/2551-0001144-9 and 16/2551-0000251-7) and Conselho Nacional de Desenvolvimento Científico e Tecnológico (302280/2019-7). MVC and GFH are grateful to Consejo Nacional de Investigaciones Científicas y Técnicas (CONICET).

6 DATA AVAILABILITY

The data underlying this article will be shared on reasonable request to the corresponding author.

REFERENCES

Abazajian K. N. et al., 2009, *ApJS*, 182, 543
 Alarie A., Morisset C., 2019, *Rev. Mex. Astron. Astrofis.*, 55, 377
 Aldrovandi S. M. V., Contini M., 1984, *A&A*, 140, 368
 Alende Prieto C., Lambert D. L., Asplund M., 2001, *ApJ*, 556, L63

Allen M. G., Groves B. A., Dopita M. A., Sutherland R. S., Kewley L. J., 2008, *ApJS*, 178, 20
 Amorín R. et al., 2012, *ApJ*, 754, L22
 Arav N., Xu X., Miller T., Kriss G. A., Plesha R., 2020, *ApJS*, 247, 37
 Baldwin J. A., Phillips M. M., Terlevich R., 1981, *PASP*, 93, 5
 Beck R., 2012, *J. Phys. Conf. Ser.*, 372, 02051
 Binette L., Dopita M. A., Tuohy I. R., 1985, *ApJ*, 297, 476
 Blanton M. R. et al., 2017, *AJ*, 154, 28
 Bosch G. et al., 2019, *MNRAS*, 489, 1787
 Bresolin F. et al., 2020, *MNRAS*, 495, 4347
 Carvalho S. P. et al., 2020, *MNRAS*, 492, 5675
 Castro C. S., Dors O. L., Cardaci M. V., Hägele G. F., 2017, *MNRAS*, 467, 1507
 Congiu E. et al., 2017, *MNRAS*, 471, 562
 Contini M., 1997, *A&A*, 483, 887
 Contini M., 2012, *MNRAS*, 425, 1205
 Contini M., 2014, *A&A*, 564, 19
 Contini M., 2017, *MNRAS*, 469, 3125
 Contini M., 2018, *A&A*, 620, 37
 Contini M., 2019, *MNRAS*, 488, 4487
 Contini M., Aldrovandi S. M. V., 1983, *A&A*, 127, 15
 Contini M., Aldrovandi S. M. V., 1986, *A&A*, 168, 41
 Contini M., Viegas S. M., 2001, *ApJSS*, 132, 211
 Cruz-Gonzalez I., Guichard J., Serrano A., Carrasco L., 1991, *PASP*, 103, 888
 Davies R. L., Rich J. A., Kewley L. J., Dopita M. A., 2014a, *MNRAS*, 439, 3835
 Davies R. L., Kewley L. J., Ho I.-T., Dopita M. A., 2014b, *MNRAS*, 444, 3961
 Denicoló G., Terlevich R., Terlevich E., 2002, *MNRAS*, 330, 69
 Dopita M. A., Sutherland R. A., 1995, *ApJ*, 455, 468
 Dopita M. A., Sutherland R. A., 1996, *ApJS*, 102, 161
 Dors O., Monteiro A. F., Cardaci M. V., Hägele G. F., Krabbe A. C., 2019, *MNRAS*, 486, 5866
 Dors O. L., Cardaci M. V., Hägele G. F., Krabbe A. C., 2014, *MNRAS*, 443, 1291
 Dors O. L., Cardaci M. V., Hägele G. F., Rodrigues I., Grebel E. K., Pilyugin L. S., Freitas-Lemes P., Krabbe A. C., 2015, *MNRAS*, 453, 4102
 Dors O. L., Arellano-Córdoba K. Z., Cardaci M. V., Hägele G. F., 2017, *MNRAS*, 468, L113
 Dors O. L., Agarwal B., Hägele G. F., Cardaci M. V., Rydberg C., Riffel R. A., Oliveira A. S., Krabbe A. C., 2018, *MNRAS*, 479, 2294
 Dors O. L. et al., 2020a, *MNRAS*, 492, 468
 Dors O. L. et al., 2020b, *MNRAS*, 496, 3209
 Dyson J. E., 1979, *A&A*, 73, 132
 Feltre A., Charlot S., Gutkin J., 2016, *MNRAS*, 456, 3354
 Ferland G. J., Netzer H., 1983, *ApJ*, 264, 105
 Ferland G. J., Osterbrock D. E., 1986, *ApJ*, 300, 658
 Ferland G. J., Truran J. W., 1980, *ApJ*, 240, 608
 Ferland G. J. et al., 2017, *Rev. Mex. Astron. Astrofis.*, 53, 385
 Flury S. R., Moran E. C., 2020, *MNRAS*, 496, 2191
 Frew D. J., Parker Q. A., 2010, *Publ. Astron. Soc. Austr.*, 27, 129
 Garnett D. R., 1992, *AJ*, 103, 1330
 Grevesse N., Sauval A. J., 1998, *Space Sci. Rev.*, 85, 161
 Groves B. A., Heckman T. M., Kauffmann G., 2006, *MNRAS*, 371, 1559
 Guo Y. et al., 2020, *ApJ*, 898, 26
 Hägele G. F. et al., 2006, *MNRAS*, 372, 293
 Hägele G. F. et al., 2008, *MNRAS*, 383, 209
 Hägele G. F., Díaz A. I., Terlevich R., Terlevich E., Bosch G. L., Cardaci M. V., 2013, *MNRAS*, 432, 810
 Harrison C. M., Costa T., Tadhunter C. N., Flütsch A., Kakkad D., Perna M., Vietri G., 2018, *Nat. Astron.*, 2, 198
 Heckman T. M., Balick B., 1979, *A&A*, 79, 350
 Henry R. C. B., Edmunds M. G., Köppen J., 2000, *ApJ*, 541, 660
 Ilha G. S. et al., 2019, *MNRAS*, 484, 252
 Ji X., Yan R., 2020, *MNRAS*, 499, 5749
 Ji X., Yan R., Riffel R., Drory N., Zhang K., 2020, *MNRAS*, 496, 1262
 Kauffmann G. et al., 2003, *MNRAS*, 341, 33

- Kewley L. J., Dopita M. A., Sutherland R. S., Heisler C. A., Trevena J., 2001, *ApJ*, 556, 121
- Kewley L. J., Jansen R. A., Geller M. J., 2005, *PASP*, 117, 227
- Kewley L. J., Groves B., Kauffmann G., Heckman T., 2006, *MNRAS*, 372, 961
- Kewley L. J., Maier C., Yabe K., Ohta K., Akiyama M., Dopita M. A., Yuan T., 2013, *ApJ*, 774, L10
- King A., Pounds K., 2015, *ARA&A*, 53, 115
- Komossa S., Schulz H., 1997, *A&A*, 323, 31
- Koski A. T., 1978, *ApJ*, 223, 56
- Kraemer S. B., Wu C.-C., Crenshaw D. M., Harrington J. P., 1994, *ApJ*, 435, 171
- Leitherer C. et al., 1999, *ApJS*, 123, 3
- Matsuoka K., Nagao T., Maiolino R., Marconi A., Taniguchi Y., 2009, *A&A*, 503, 721
- Matsuoka K. et al., 2018, *A&A*, 616, L4
- May D., Rodríguez-Ardila A., Prieto M. A., Fernández-Ontiveros J. A., Diaz Y., Mazzalay X., 2018, *MNRAS*, 481, L105
- Melnick J., 1977, *ApJ*, 213, 15
- Mignoli M. et al., 2019, *A&A*, 626, 9
- Nagao T., Murayama T., Taniguchi Y., 2001, *ApJ*, 549, 155
- Nagao T., Maiolino R., Marconi A., 2006, *A&A*, 447, 863
- Nakajima K. et al., 2018, *A&A*, 612, 94
- Pérez-Montero E., 2014, *MNRAS*, 441, 2663
- Pérez-Montero E., Contini T., 2009, *MNRAS*, 398, 949
- Pérez-Montero E. et al., 2013, *A&A*, 549, 25
- Pérez-Montero E., Dors O. L., Vilchez J. M., García-Benito R., Cardaci M. V., Hagele G. F., 2019, *MNRAS*, 489, 2652
- Pilyugin L. S., 2003, *A&A*, 399, 1003
- Pilyugin L. S., Grebel E. K., 2016, *MNRAS*, 457, 3678
- Pilyugin L. S., Grebel E. K., Mattsson L., 2012, *MNRAS*, 424, 2316
- Relaño M., Beckman J. E., Zurita A., Rozas M., Giammanco C., 2005, *A&A*, 431, 235
- Riffel R. A., Storchi-Bergmann T., Riffel R., 2014, *ApJ*, 780, L24
- Riffel R. A., Storchi-Bergmann T., Zakamska N. L., Riffel R., 2020, *MNRAS*, 496, 4857
- Rosario D. J., Whittle M., Nelson C. H., Wilson A. S., 2010, *ApJ*, 711, L94
- Rozas M., Richer M. G., Steffen W., Garcí-Segura G., López J. A., 2007, *A&A*, 467, 603
- Skillman E. D., Balick B., 1984, *ApJ*, 280, 580
- Spence R. A. W. et al., 2016, *MNRAS*, 459, L16
- Stasińska G., 1984, *A&A*, 135, 341
- Storchi-Bergmann T., Pastoriza M. G., 1990, *PASP*, 102, 1359
- Storchi-Bergmann T., Schmitt H. R., Calzetti D., Kinney A. L., 1998, *AJ*, 115, 909
- Tadhunter C. N., 1991, *MNRAS*, 215, 46
- Thomas A. D., Kewley L. J., Dopita M. A., Groves B. A., Hopkins A. M., Sutherland R. S., 2018, *ApJ*, 861, L2
- Thomas A. D., Kewley L. J., Dopita M. A., Groves B. A., Hopkins A. M., Sutherland R. S., 2019, *ApJ*, 874, 100
- Vaona L., Ciroi S., Di Mille F., Cracco V., La Mura G., Rafanelli P., 2012, *MNRAS*, 427, 1266
- Veilleux S., Osterbrock D. E., 1987, *ApJS*, 63, 295
- Viegas-Aldrovandi S. M., Contini M., 1989, *ApJ*, 339, 689
- Vila-Costas M. B., Edmunds M. G., 1993, *MNRAS*, 265, 199
- Westmoquette M. S., Exter K. M., Smith L. J., Gallagher J. S., 2007, *MNRAS*, 381, 894
- Wylezalek D., Flores A. M., Zakamska N. L., Greene J. E., Riffel R. A., 2020, *MNRAS*, 492, 4680
- York D. G. et al., 2000, *ApJ*, 120, 1579
- Zhang Z. T., Liang Y. C., Hammer F., 2013, *MNRAS*, 430, 2605

SUPPORTING INFORMATION

Supplementary data are available at *MNRAS* online.

Table2.dat

Table1.dat

Please note: Oxford University Press is not responsible for the content or functionality of any supporting materials supplied by the authors. Any queries (other than missing material) should be directed to the corresponding author for the article.

This paper has been typeset from a \LaTeX file prepared by the author.